

Human-induced greening of the northern extratropical land surface

Jiafu Mao^{1*}, Aurélien Ribes², Binyan Yan³, Xiaoying Shi¹, Peter E. Thornton¹, Roland Séférian², Philippe Ciais⁴, Ranga B. Myneni⁵, Hervé Douville², Shilong Piao^{6,7,8}, Zaichun Zhu⁶, Robert E. Dickinson³, Yongjiu Dai⁹, Daniel M. Ricciuto¹, Mingzhou Jin¹⁰, Forrest M. Hoffman¹¹, Bin Wang^{12,13}, Mengtian Huang⁶ and Xu Lian⁶

Significant land greening in the northern extratropical latitudes (NEL) has been documented through satellite observations during the past three decades^{1–5}. This enhanced vegetation growth has broad implications for surface energy, water and carbon budgets, and ecosystem services across multiple scales^{6–8}. Discernible human impacts on the Earth's climate system have been revealed by using statistical frameworks of detection-attribution^{9–11}. These impacts, however, were not previously identified on the NEL greening signal, owing to the lack of long-term observational records, possible bias of satellite data, different algorithms used to calculate vegetation greenness, and the lack of suitable simulations from coupled Earth system models (ESMs). Here we have overcome these challenges to attribute recent changes in NEL vegetation activity. We used two 30-year-long remote-sensing-based leaf area index (LAI) data sets^{12,13}, simulations from 19 coupled ESMs with interactive vegetation, and a formal detection and attribution algorithm^{14,15}. Our findings reveal that the observed greening record is consistent with an assumption of anthropogenic forcings, where greenhouse gases play a dominant role, but is not consistent with simulations that include only natural forcings and internal climate variability. These results provide the first clear evidence of a discernible human fingerprint on physiological vegetation changes other than phenology and range shifts¹¹.

This study examines the growing season LAI over the NEL (30–75° N). The LAI is a measurable biophysical parameter using satellite observation, an archived prognostic variable of the Coupled Model Intercomparison Project Phase 5 (CMIP5) ESMs, and a direct indicator of the leaf surface per unit ground area that exchanges energy, water, carbon dioxide and momentum with the planetary boundary layer. We employed the recently published LAI3g data set¹² and the GEOLAND2 LAI data¹³, both of which were quality-controlled over the NEL region for the 1982–2011 period (Supplementary Information 1). We compared the observed

changes of LAI to simulated variations from multi-model results obtained from the CMIP5 archive (Supplementary Information 2 and Supplementary Table 1). These ensemble simulations comprise ALL, with historical anthropogenic and natural forcings, GHG, with greenhouse gases forcing only, NAT, with natural forcing only, CTL, with internal variability (IV) only, esmFixClim2, with CO₂ physiological effects, and esmFdbk2, with greenhouse gases radiative effects. Beyond the standard comparison of time series and patterns of trends, two methods were applied to detect and attribute changes in observed LAI, including a formal 'optimal fingerprint' analysis (Methods).

From 1982 to 2011, LAI3g, GEOLAND2 and their mean exhibited greening trends over the NEL vegetated area (85.3%, 69.5% and 80.6%, respectively), except across a narrow latitudinal band over Canada and Alaska, and in a few spots over Eurasia (Fig. 1a–c). The largest positive increase is observed in western Europe and eastern North America for both LAI products, consistent with previous results^{1–5}. The multi-model ensemble-mean LAI changes under NAT forcing had negative trends (browning) across vast areas of North America (51.9% of North America vegetated area) and smaller positive trends over Eurasia (80.8% of Eurasia vegetated area) than in the averaged satellite observations (86.8% of Eurasia vegetated area) (Fig. 1d). By contrast, the trend from the ALL ensemble mean is closer to observations (Fig. 1e). The spatial distribution of observed LAI trends was also captured well by the ensemble-mean GHG-only simulations (Fig. 1f). This indicates that the combined anthropogenic effects, particularly the well-mixed greenhouse gases, have contributed largely to widespread greening trends of the NEL for the past three decades. Similar results are obtained for the 1982–2011 period when different definitions of growing season are chosen (Supplementary Fig. 1).

In the NEL, the two remotely sensed LAI anomalies showed a large interannual variability superimposed on an overall increasing trend (Fig. 2). These observed trends agree with those found in the

¹Environmental Sciences Division and Climate Change Science Institute, Oak Ridge National Laboratory, Oak Ridge, Tennessee 37831-6301, USA. ²Centre National de Recherches Météorologiques, Météo-France/CNRS, 42 Avenue Gaspard Coriolis, 31057 Toulouse, France. ³Jackson School of Geosciences, the University of Texas, Austin, Texas 78712-1692, USA. ⁴Laboratoire des Sciences du Climat et de l'Environnement, LSCE, 91191 Gif sur Yvette, France.

⁵Department of Earth and Environment, Boston University, Boston, Massachusetts 02215, USA. ⁶Sino-French Institute for Earth System Science, College of Urban and Environmental Sciences, Peking University, Beijing 100871, China. ⁷Key Laboratory of Alpine Ecology and Biodiversity, Institute of Tibetan Plateau Research, Chinese Academy of Sciences, Beijing 100085, China. ⁸CAS Center for Excellence in Tibetan Plateau Earth Science, Beijing 100085, China. ⁹College of Global Change and Earth System Science, Beijing Normal University, Beijing 100875, China. ¹⁰Department of Industrial and Systems Engineering, University of Tennessee, Knoxville, Tennessee 37996-2315, USA. ¹¹Computer Science and Mathematics Division and Climate Change Science Institute, Oak Ridge National Laboratory, Oak Ridge, Tennessee 37831, USA. ¹²State Key Laboratory of Numerical Modeling for Atmospheric Sciences and Geophysical Fluid Dynamics, Institute of Atmospheric Physics, Beijing 100029, China. ¹³Center for Earth System Science, Tsinghua University, Beijing 100084, China. *e-mail: maoj@ornl.gov

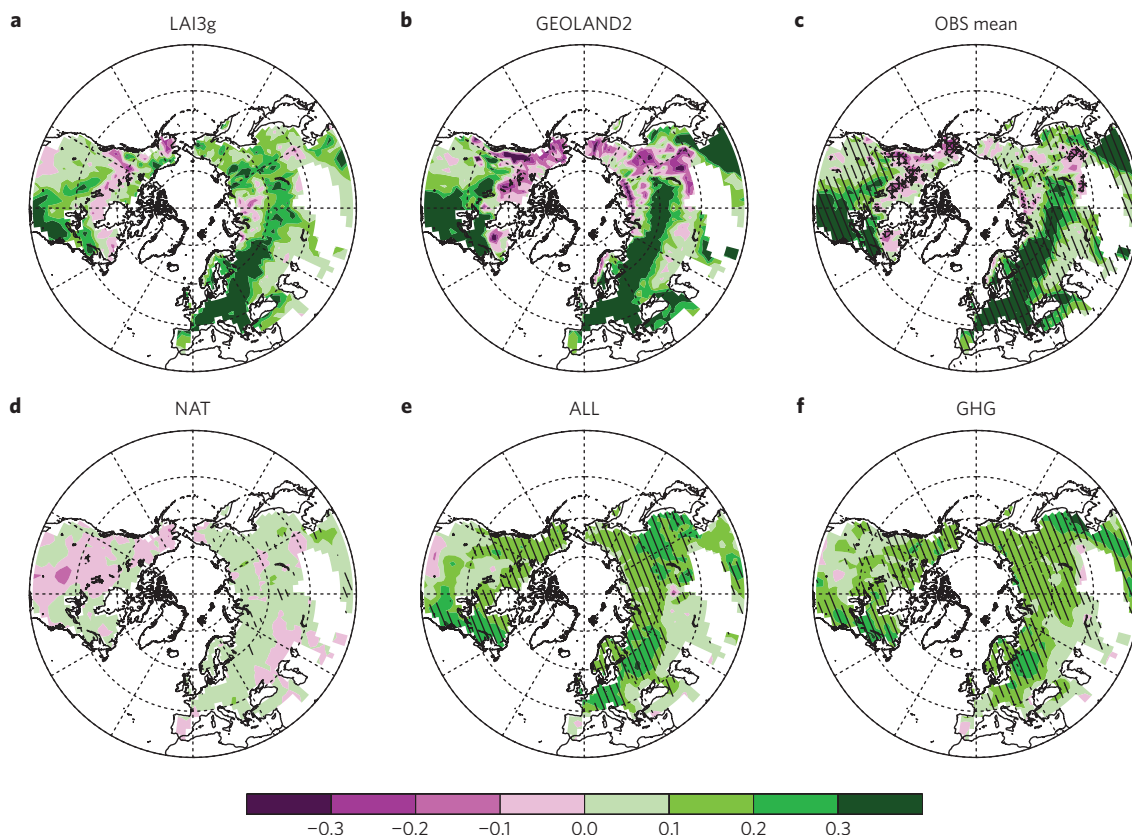


Figure 1 | Spatial distribution of LAI trends for 1982–2011. **a–f**, Spatial distribution of the linear trends in the growing season (April–October) LAI ($\text{m}^2 \text{m}^{-2}$ per 30 yr) in LAI3g product (**a**), GEOLAND2 product (**b**), the mean of LAI3g and GEOLAND2 (OBS mean) (**c**), CMIP5 simulations with natural forcings alone (NAT) (**d**), CMIP5 simulations with anthropogenic and natural forcings (ALL) (**e**) and CMIP5 simulations with greenhouse gas forcings (GHG) (**f**). The hatched area in **c** indicates that both satellite-based LAI data sets agree on the increasing trend of LAI, and the area with black crosses indicates that both satellite-based LAI data sets agree on the decreasing trend of LAI. The hatched area in **d–f** indicates that at least 90% of the simulation members agree on the increasing trend of LAI; the area with black crosses indicates that at least 90% of the simulation members agree on the decreasing trend of LAI.

ALL and GHG ensembles, but were much larger than those simulated in the NAT ensemble (Fig. 2 and Supplementary Figs 2 and 3).

Many observed values fall well outside the simulated 5th–95th percentiles associated with individual NAT realizations, suggesting a clear inconsistency between observations and this ensemble. The observations, however, are much more consistent with the multi-model ensembles that are forced by the human-caused increases of greenhouse gases. The comparison of the 1982–2011 observed trends ($+0.143$, $+0.163$ and $+0.153 \text{ m}^2 \text{m}^{-2}$ per 30 yr for LAI3g, GEOLAND2, and their average) with a set of 30-year segments from pre-industrial control simulations (Fig. 3a) confirms that the observed trends significantly exceed the range of values expected from IV only under a stationary climate ($\pm 0.066 \text{ m}^2 \text{m}^{-2}$ per 30 yr, p -value $< 10^{-4}$) (Supplementary Information 3). These observed trends also do not agree with trends in the NAT ensemble (Fig. 3b, p -value $< 10^{-4}$), which, on average, is positive but much smaller ($+0.017 \pm 0.054 \text{ m}^2 \text{m}^{-2}$ per 30 yr, or $+0.017 \pm 0.066 \text{ m}^2 \text{m}^{-2}$ per 30 yr if the broadest IV estimate is used). In contrast, the observed trends are consistent with those in the ALL ensemble (Fig. 3a, $+0.133 \pm 0.089 \text{ m}^2 \text{m}^{-2}$ per 30 yr, p -value = 0.64) as well as GHG ensemble (Fig. 3b, $+0.129 \pm 0.120 \text{ m}^2 \text{m}^{-2}$ per 30 yr, p -value = 0.67). Similar results can be found with different definitions of the growing season (Supplementary Fig. 4). According to the definitions used in IPCC Fourth Assessment Report (AR4)⁹, this analysis allows us to attribute at least part of the observed LAI changes to human influence because the trends are detectable, consistent with the expected response to all forcings,

and inconsistent with the expected response to natural forcings only (that is, alternative, physically plausible causes).

A more comprehensive and formal method used in IPCC Fifth Assessment Report (AR5)¹⁰ for attributing observed changes involves an optimized regression of observations onto the expected response from models to one or several external forcings (Methods). The main output from this type of analysis is the scaling factor β , which scales the model's responses to best fit the observations. Assessing whether the unexplained signal (that is, the residuals of the regression) is consistent with IV is also a key diagnosis in this method. This diagnosis is usually achieved using a residual consistency test (RCT). We applied the detection and attribution (D&A) algorithm^{14,15}, to the ALL and GHG-only temporal response patterns of three-year-mean LAI (as in Fig. 2), respectively. We considered the average of all CMIP5 models in Multi1 (only one simulation from each model) and the average of the models with larger ensembles in Multi3 (that is, models with at least three members) (Supplementary Table 1). The observed LAI change over 1982–2011 is found to be significant, as β scaling factors are significantly larger than 0 (Fig. 4). The 90% confidence intervals of β include 1, which means that the observations are consistent with models, in terms of the magnitude of the forced ALL and GHG-only responses. These two results are fairly robust if response patterns from individual models or individual observed data sets are considered. However, the RCT is strongly rejected in most cases, even if all forcings are included, indicating that the residuals of the fit are much larger than those expected from the simulated IV.

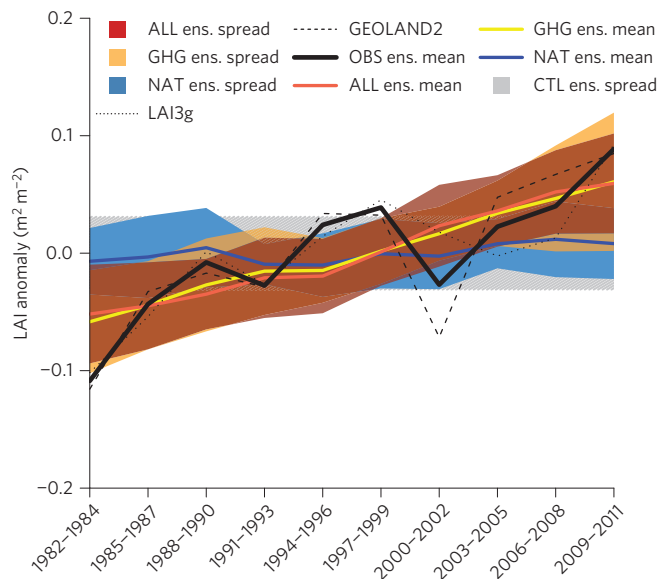


Figure 2 | Observed and simulated 1982–2011 time series of LAI anomalies. The three-year-mean growing season (April–October) LAI anomalies over land of the NEL for both LAI3g and GEOLAND2 satellite-derived observations, for CMIP5 simulations accounting for solely natural (NAT) and greenhouse gas forcings (GHG), as well as CMIP5 simulations accounting for both anthropogenic and natural forcings (ALL). The ensemble (ens.) mean for each set of forcings is given in blue, yellow, and red solid lines for NAT, GHG, and ALL, respectively. Individual satellite-derived observations are indicated with dashed black lines; the observational average is given with a bold solid black line. Blue, yellow, and red shading represent the 5%–95% confidence interval for NAT, GHG, and ALL ensembles, respectively (computed assuming a Gaussian distribution). The grey-hatched area represents the 5–95% confidence interval for the range of variability for the centennial-long pre-industrial unforced control simulations (CTL).

To deal with a possible underestimation of IV by ESMs, we tested the robustness of those key results to several inflated IV assumptions (Supplementary Information 4). Detection was found to occur with all values of IV variance that are consistent with observations, and

even IV multiplied by a factor as large as 8, which strongly reinforces confidence in our results.

With the human influence on recent evolution of NEL vegetation activity established, we are now in a position to discuss the possible mechanisms behind those human influences (for example, the impacts of nitrogen deposition, land use/land cover change (LULCC), and the CO₂-induced physiological versus the GHG-induced climate effects) on LAI changes. We analysed a smaller subset of CMIP5 ensemble models representing mechanisms of interest without using the D&A methodology (Supplementary Table 1). D&A techniques are not useful for discriminating between these forcings, as the corresponding signals are usually too collinear over time, leading to a signal-to-noise ratio that is too small. For the ALL simulations, models including the nitrogen cycle exhibited higher LAI trends than those lacking explicit nitrogen cycles, reflecting in part a human influence from increased nitrogen deposition (Supplementary Fig. 7a,b). Consistent with the results of offline land surface models including carbon–nitrogen dynamics (for example, Fig. 4c in ref. 4), the difference seen in the ESMs is particularly strong over eastern North America and eastern Asia, areas of known high levels of human-caused nitrogen deposition¹⁶. The nitrogen-enabled models appear to capture observed LAI trends in these regions (Fig. 1c). Slightly negative LAI trends observed over southwest North America, western Canada, and spots of Eurasia seemed to correspond to the LULCC-induced vegetation browning at the same locations (Fig. 1c and Supplementary Fig. 7e). Nonetheless, the net LULCC-induced LAI changes from CanESM2, the only model providing LULCC-only simulations, were fairly small (Supplementary Fig. 9). CO₂ fertilization stimulated the vegetation growth over large areas of the NEL (83.8% vegetated area) except in central North America (Supplementary Fig. 7f). The response of modelled LAI to GHG-forced climate change shows regions of decrease that coincide mainly with reduced precipitation and regions of increase that coincide with regions of higher precipitation and warmer temperatures (Supplementary Figs 7g and 8).

Previous work assessing modelled and observed LAI has focused on phenological variation, interannual variability, and multiyear trends; spatiotemporal changes in LAI were attributed to variation in climate drivers (mainly temperature and precipitation)^{17–21}. This study adds to an increasing body of evidence that the NEL has experienced an enhancement of vegetation activity, as reflected by

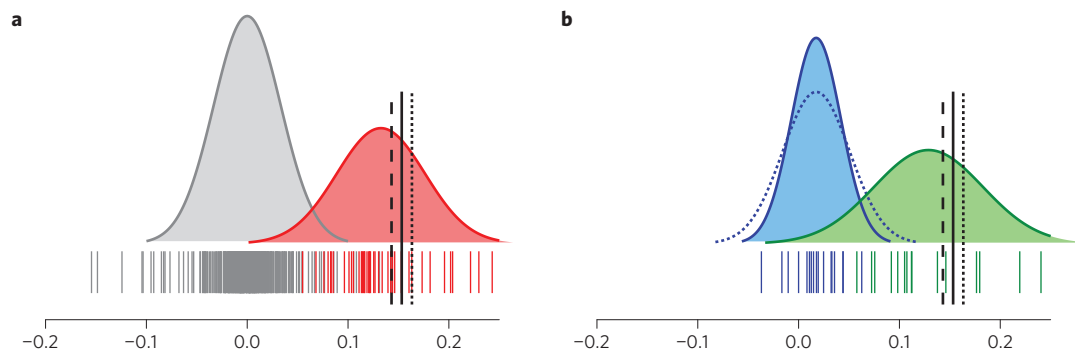


Figure 3 | Parameterized frequency distributions of LAI 1982–2011 30-year-long trends. **a, b,** Comparison of the observed trends ($m^2 m^{-2}$ per 30 yr) over land of the NEL from both LAI3g and GEOLAND2 satellite-derived observations, against the Gaussian-fitted probability density function (pdf) of simulated trends from CMIP5 simulations accounting for unforced pre-industrial control variability (CTL, in grey), solely natural forcings (NAT, in blue) and greenhouse gas forcings (GHG, in green), as well as CMIP5 simulations accounting for both anthropogenic and natural forcings (ALL, in red). Individual satellite-derived observations are indicated with long and short vertical dashed black lines for LAI3g and GEOLAND2, respectively; the observational average is given with a bold solid black line. **a,** Comparison between trends as estimated from satellite-derived products and as simulated from both individual 30-year segments taken from the CTL simulations and historical ALL simulations. **b,** Comparison between trends as estimated from satellite-derived products and as simulated from NAT and GHG simulations. The dotted blue line, representing the pdf, corresponds to the NAT pdf, but using a variance equal to that diagnosed from the CTL ensemble.

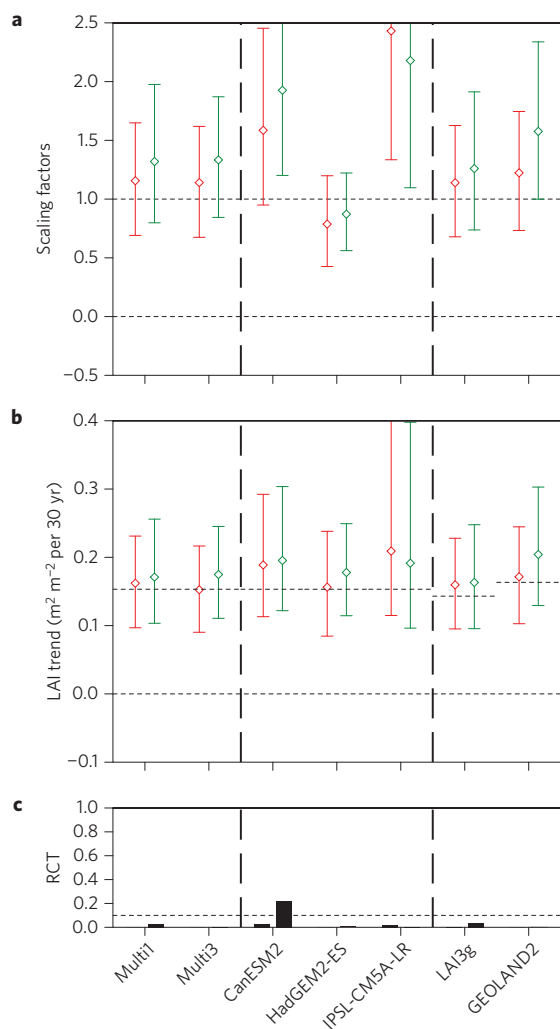


Figure 4 | Results from optimal D&A for 1982–2011 time series of LAI anomalies. **a–c**, The D&A analysis was performed over land of the NEL on ensemble-mean 1982–2011 time series of LAI anomalies. Response patterns were derived from CMIP5 simulations accounting for both anthropogenic and natural forcings (ALL, in red), or greenhouse gas forcings only (GHG, in green), in a one-signal detection analysis. The observational average of LAI3g and GEOLAND2 was used as reference in the analysis. Scaling factors (β —see text) best estimates and their 90% confidence intervals (**a**), attributable trends over the 30-year-long time series (**b**) and p -value of the residual consistency test (RCT) (**c**) are shown. Results were obtained from a total least square (TLS) analysis using the multi-model mean or selected individual model responses. ‘Multi1’ and ‘Multi3’ refer to two different CMIP5 ensemble means (see text). Observational uncertainty was assessed using individual satellite-derived observations (LAI3g or GEOLAND2) regressed onto the Multi1 response pattern.

increased trends in vegetation indices^{1–5}, aboveground vegetation biomass^{6,7}, and terrestrial carbon fluxes²² during the satellite era. Our analysis goes beyond previous studies by using D&A methods to establish that the trend of strengthened northern vegetation greening is clearly distinguishable from both IV and the response to natural forcings alone. It can be rigorously attributed, with high statistical confidence, to anthropogenic forcings, particularly to rising atmospheric concentrations of greenhouse gases. As an attempt to decipher which mechanisms are behind those trends, we further analysed the contribution of nitrogen deposition, LULCC, CO₂ fertilization and GHG-induced climate change to the NEL vegetation growth. This provides potential leads to understanding

the geographic structure of the vegetation response to selected anthropogenic forcing agents.

An accurate quantification of the responses to individual human and natural drivers, however, needs more research efforts, owing to uncertainties associated with the ESMs, weaknesses of the CMIP5 experimental design, and limitations in the observations. Relative to the observations, the simulations with ALL and GHG forcings illustrated relatively weaker interannual variability of vegetation growth (Fig. 2 and Supplementary Figs 2 and 3). This discrepancy may arise from structural errors of the land component in the ESMs (for example, weak or no representation of vegetation mortality, disturbance and successional dynamics)^{23–25}. Because spatial and temporal patterns of vegetation growth are tightly coupled with precipitation variability^{4,17,18}, the underestimation could also arise from the reported underestimation of interannual precipitation variability in CMIP models over Northern Hemisphere land^{16,27}. Multi-model ensemble means can have persistent biases, such as overprediction of growing season length due to advanced spring growth and delayed autumn senescence in Northern Hemisphere temperate ecosystems^{17,28}. If such a phenological bias were changing steadily over time, it could influence estimation of LAI trends reported here. We mitigate against this type of bias by comparing our results for different seasonal periods. Because our results are consistent for different definitions of growing season (Supplementary Figs 1–4 and 6), early and late season model biases, to the extent they are present in our multi-model data set, seem to be stationary in time. Understanding and ranking the multiple reasons for deficiencies in CMIP5 simulations, however, remain extremely difficult, given the lack of global LAI simulations with land surface models driven by common observed environmental forcings. Such an obstacle should be overcome in the next phase of CMIP, which will include an international intercomparison of the land surface components from the participating ESMs²⁹. Long-term remote-sensing data are often contaminated by clouds and snow cover, and are impacted by the change of satellites³⁰. For example, the LAI3g data set was probably influenced in 1991 by the eruption of Mount Pinatubo and subsequent loss of orbit by NOAA 11, seen particularly in the world’s forests¹²; the merging of reflectance information from different satellites during the pre- and post-2000 periods for both LAI3g and GEOLAND2 products has the potential to cause inhomogeneity in the data^{12,13}. These observational uncertainties, which are not considered here, might artificially increase the observed interannual variability. Our sensitivity tests, however, show that our key findings are robust to these issues, and the fingerprint patterns assessed by the ALL and GHG ensembles can still be identified quantitatively in the relatively short instrumental record.

Given the strong evidence provided here of historical human-induced greening in the northern extratropics, society should consider both intended and unintended consequences of its interactions with terrestrial ecosystems and the climate system.

Methods

Methods and any associated references are available in the [online version of the paper](#).

Received 13 August 2015; accepted 16 May 2016; published online 27 June 2016

References

- Myneni, R. B., Keeling, C., Tucker, C., Asrar, G. & Nemani, R. Increased plant growth in the northern high latitudes from 1981 to 1991. *Nature* **386**, 698–702 (1997).
- Zhou, L. *et al.* Variations in northern vegetation activity inferred from satellite data of vegetation index during 1981 to 1999. *J. Geophys. Res.* **106**, 20069–20083 (2001).
- Lucht, W. *et al.* Climatic control of the high-latitude vegetation greening trend and Pinatubo effect. *Science* **296**, 1687–1689 (2002).

4. Mao, J. *et al.* Global latitudinal-asymmetric vegetation growth trends and their driving mechanisms: 1982–2009. *Remote Sens.* **5**, 1484–1497 (2013).
5. Buitenwerf, R., Rose, L. & Higgins, S. I. Three decades of multi-dimensional change in global leaf phenology. *Nature Clim. Change* **5**, 364–368 (2015).
6. Pan, Y. *et al.* A large and persistent carbon sink in the world's forests. *Science* **333**, 988–993 (2011).
7. Liu, Y. Y. *et al.* Recent reversal in loss of global terrestrial biomass. *Nature Clim. Change* **5**, 470–474 (2015).
8. Ukkola, A. M. *et al.* Reduced streamflow in water-stressed climates consistent with CO₂ effects on vegetation. *Nature Clim. Change* **6**, 75–78 (2015).
9. Hegerl, G. C. *et al.* in *Climate Change 2007: The Physical Science Basis* (eds Solomon, S. *et al.*) 667–732 (IPCC, Cambridge Univ. Press, 2007).
10. Bindoff, N. L. *et al.* in *Climate Change 2013: The Physical Science Basis* (eds Stocker, T. F. *et al.*) 867–931 (IPCC, Cambridge Univ. Press, 2013).
11. Cramer, W. *et al.* in *Climate Change 2014: Impacts, Adaptation, and Vulnerability* (eds Field, C. B. *et al.*) 979–1037 (IPCC, Cambridge Univ. Press, 2014).
12. Zhu, Z. *et al.* Global data sets of vegetation leaf area index (LAI) 3g and fraction of photosynthetically active radiation (FPAR) 3g derived from global inventory modeling and mapping studies (GIMMS) normalized difference vegetation index (NDVI3g) for the period 1981 to 2011. *Remote Sens.* **5**, 927–948 (2013).
13. Baret, F. *et al.* GEOV1: LAI and FAPAR essential climate variables and FCOVER global time series capitalizing over existing products. Part 1: Principles of development and production. *Remote Sens. Environ.* **137**, 299–309 (2013).
14. Allen, M. & Stott, P. Estimating signal amplitudes in optimal fingerprinting, part I: theory. *Clim. Dynam.* **21**, 477–491 (2003).
15. Ribes, A., Planton, S. & Terray, L. Application of regularised optimal fingerprinting to attribution. part I: method, properties and idealised analysis. *Clim. Dynam.* **41**, 2817–2836 (2013).
16. Lamarque, J. F. *et al.* Multi-model mean nitrogen and sulfur deposition from the Atmospheric Chemistry and Climate Model Intercomparison Project (ACCMIP): evaluation of historical and projected future changes. *Atmos. Chem. Phys.* **13**, 7997–8018 (2013).
17. Anav, A. *et al.* Evaluation of land surface models in reproducing satellite derived leaf area index over the high-latitude northern hemisphere. part II: Earth system models. *Remote Sens.* **5**, 3637–3661 (2013).
18. Mahowald, N. *et al.* Projections of leaf area index in Earth system models. *Earth Syst. Dynam.* **7**, 211–229 (2016).
19. Menzel, A. *et al.* European phenological response to climate change matches the warming pattern. *Glob. Change Biol.* **12**, 1969–1976 (2006).
20. Zeng, F., Collatz, G., Pinzon, J. & Ivanoff, A. Evaluating and quantifying the climate-driven interannual variability in Global Inventory Modeling and Mapping Studies (GIMMS) Normalized Difference Vegetation Index (NDVI3g) at global scales. *Remote Sens.* **5**, 3918–3950 (2013).
21. Piao, S. *et al.* Evidence for a weakening relationship between interannual temperature variability and northern vegetation activity. *Nature Commun.* **5**, 5018 (2014).
22. Anav, A. *et al.* Spatio-temporal patterns of terrestrial gross primary production: a review. *Rev. Geophys.* **53**, 785–818 (2015).
23. McDowell, N. G. *et al.* Multi-scale predictions of massive conifer mortality due to chronic temperature rise. *Nature Clim. Change* **6**, 295–300 (2016).
24. Di Vittorio, A. V. *et al.* From land use to land cover: restoring the afforestation signal in a coupled integrated assessment–Earth system model and the implications for CMIP5 RCP simulations. *Biogeosciences* **11**, 6435–6450 (2014).
25. Kunstler, G. *et al.* Plant functional traits have globally consistent effects on competition. *Nature* **529**, 204–207 (2016).
26. Zhang, X. *et al.* Detection of human influence on twentieth-century precipitation trends. *Nature* **448**, 461–465 (2007).
27. Wu, P., Christidis, N. & Stott, P. Anthropogenic impact on Earth's hydrological cycle. *Nature Clim. Change* **3**, 807–810 (2013).
28. Keenan, T. F. *et al.* Net carbon uptake has increased through warming-induced changes in temperate forest phenology. *Nature Clim. Change* **4**, 598–604 (2014).
29. Eyring, V. *et al.* Overview of the Coupled Model Intercomparison Project Phase 6 (CMIP6) experimental design and organization. *Geosci. Model. Dev. Discuss.* **8**, 10539–10583 (2015).
30. Pinzon, J. E. & Tucker, C. J. A non-stationary 1981–2012 AVHRR NDVI3g time series. *Remote Sens.* **6**, 6929–6960 (2014).

Acknowledgements

This work is supported by the Biogeochemistry–Climate Feedbacks Scientific Focus Area project funded through the Regional and Global Climate Modeling Program, and the Terrestrial Ecosystem Science Scientific Focus Area project funded through the Terrestrial Ecosystem Science Program, with additional support from the Accelerated Climate Modeling for Energy project, in the Climate and Environmental Sciences Division (CESD) of the Biological and Environmental Research (BER) Program in the US Department of Energy Office of Science. Oak Ridge National Laboratory is managed by UT-BATTELLE for DOE under contract DE-AC05-00OR22725. This work is supported in part by the Fondation STAE, via the project Chavana. R.S. thanks the H2020 project CRESCENDO 'Coordinated Research in Earth Systems and Climate: Experiments, Knowledge, Dissemination and Outreach', which received funding from the European Union's Horizon 2020 research and innovation programme under grant agreement no. 641816. R.B.M. is supported by NASA Earth Science Division through MODIS and VIIRS grants. B.W. is supported by the National Basic Research Program of China (Grant no. 2014CB441302). P.C. thanks the ERC SyG project IMBALANCE-P Effects of phosphorus limitations on Life, Earth system and Society Grant agreement no. 610028.

Author contributions

J.M. conceived the study. J.M., A.R., B.Y., X.S., P.E.T. and R.S. performed diagnostics and wrote the text, with comments and edits from all authors.

Additional information

Supplementary information is available in the [online version of the paper](#). Reprints and permissions information is available online at www.nature.com/reprints. Correspondence and requests for materials should be addressed to J.M.

Competing financial interests

The authors declare no competing financial interests.

Methods

Detection and attribution. Two distinct statistical approaches were used to detect and attribute the LAI changes in this study. The simple comparison of observed and simulated LAI trends (Fig. 3) is based on a simple T -test, which is further discussed in Supplementary Information 3. Then a more conventional D&A analysis is based on an optimal regression technique in which observations Y are regressed onto the expected response to historical forcing changes X^* (that is, $Y = X^* \beta + \varepsilon$, where ε denotes IV)^{14,15,31}. The scaling factors β are fitted using a total least square (TLS) approach, where the expected response X^* is estimated from model-simulated responses X , which are also contaminated by IV within the model simulation, $X = X^* + \varepsilon x$. The model is fitted following the method in ref. 15. The scaling factor β describes how the expected response has to be scaled to best match observations. Conclusions in terms of the D&A are based on the best-estimate and confidence interval on β . Attributable trends (that is, the trends explained by the external

forcing under scrutiny)³² are derived by multiplying the model-simulated trend and the estimated scaling factor $\hat{\beta}$. Similarly, upper and lower bounds of attributable trends are derived from the corresponding upper and lower bounds of β . We applied these statistical methods to the NEL average of three-year-mean LAI, as shown in Fig. 2. Natural internal variability is evaluated from unforced control simulations from several CMIP5 climate models, and expected response patterns are also taken from CMIP5 models (Supplementary Table 1).

References

31. Allen, M. R. & Tett, S. F. Checking for model consistency in optimal fingerprinting. *Clim. Dynam.* **15**, 419–434 (1999).
32. Stott, P. A. *et al.* Observational constraints on past attributable warming and predictions of future global warming. *J. Clim.* **19**, 3055–3069 (2006).